Volume-Resolved Nanostructure Survey of a Polymer Part by Means of SAXS Microtomography

Norbert Stribeck[1]*, Armando Almendarez Camarillo[1], Ulrich Nöchel[1],
Christian Schroer[2], Marion Kuhlmann[2], Stephan V. Roth[2], Rainer Gehrke[2]
Rüdiger K. Bayer[3]

[1]Institute of Technical and Macromolecular Chemistry, University of Hamburg,
Bundesstr. 45, 20146 Hamburg, Germany.
FAX: +49-40-42838-6008. E-mail: Norbert.Stribeck@desy.de
[2]HASYLAB at DESY, Notkestr. 85, 22603 Hamburg, Germany
[3]Institut für Werkstofftechnik, Universität GH Kassel, 34109 Kassel, Germany

SUBMITTED TO MACROMOL. CHEM. PHYS. 28 MAR 2006

Keywords: fibers; injection molding; microstructure; microtomography (micro-CT); small-angle X-ray scattering (SAXS)

Abstract

Small-angle X-ray scattering (SAXS) microtomography (micro-CT) resolves structure variation in an anisotropic polyethylene (PE) gradient material with fiber symmetry. 4900 reconstructed SAXS patterns describe the nanostructure as a function of volume element position in the scanned fiber cross-section. Reconstruction errors are observed. Their first-order effect is eliminated by transformation of the SAXS into a multidimensional chord distribution (CDF). Its analysis shows oriented lamellae stacks in a shell layer and extended chains in the central core of the fiber. We document zones of uni- and bimodal structure, variation of long periods, stack heights and lateral domain extension.

1 Introduction

A classical method for the non-destructive study of polymer nanostructure is the small-angle X-ray scattering (SAXS). If a polymer part is conventionally irradiated by an X-ray beam, the recorded pattern is an integral superposition of all the SAXS patterns emerging from the sequence of volume elements along the beam path. From the mathematical point of view such a superposition is a projection. A single projection is of little use for the study of nanostructure gradients in materials. As a historical resort the material has been sliced mechanically [1, 2], and every slice had to be studied by SAXS. As a matter of fact, the applicability of this method is limited because a spatial thickness resolution below 300 μm is not realistic for SAXS studies. On the other hand, the lateral spatial resolution can be diminished by means of microbeam optics [3–5]. At the synchrotron beamlines of HASYLAB, Hamburg a microbeam has not been available for scattering studies of soft matter until recently X-ray focusing beryllium lenses [6–17] have been introduced.

As the diameter of the primary beam is demagnified to several micrometers, the mechanical slicing of the material can advantageously be replaced by a mathematical treatment of recordable projected scattering data based on the Fourier slice-theorem. In a respective microtomography (micro-CT) [18] experiment a complete set of projections from a cross-section of the sample is recorded by rotating and translating the specimen with respect to the microbeam.

In the conventional micro-CT, tomographic images can be generated from many different imaging signals – including scattering data [19–21]. The conventional image itself is generated by deriving a grayscale value or a pseudo-colour from the recorded imaging signal. This signal is a function of the position of the corresponding volume element (voxel) in the reconstructed slice. In our first paper on the SAXS micro-CT experiment from a polymer part [21] we have pursued this classical route in order to retrieve a high-contrast image from the reconstructed SAXS pattern. By doing so the studied fibre cross-section has been converted into an image showing almost circular zones that are evocative of annular rings.

In summary, at HASYLAB the actually available synchrotron beamline technology for SAXS micro-CT permits to reconstruct a three-dimensional (3D) image of a sample with a spatial resolution of 57 μm. In comparison, if an absorption-sensitive commercial X-ray microscanner is employed, the spatial resolution is tenfold [22]. Even more, the tomographic analysis of a set of transmission electron microscopic (TEM) images from “thick” samples (TEMT) [23–25] permits to reconstruct nanostructure directly in 3D. Where in this setting is SAXS micro-CT unique? For many polymer parts including our sample the X-ray absorption is constant [21]. Thus the corresponding tomogram is featureless. TEMT, on the other hand, is destructive and not suited to study relatively slow spatial variations of nanometre-size structure on a micrometre scale. As we intend to demonstrate, in this field of materials science SAXS micro-CT has the potential to become a powerful tool. Compared to absorption tomograms the tomographic reconstruction of scattering images is quite involved and an analytical solution is only available, if the irradiated material shows fibre symmetry [21].

After the SAXS has been measured in a micro-CT setup and the slice reconstruction has been performed, a SAXS pattern is available for every voxel of the studied cross-section of the part. In the present work we, for the first time, analyse the reconstructed SAXS patterns quantitatively as a function of spatial position in the studied part by means of the multidimensional CDF method [26]. By doing so we intend to gather information on the variation of the semicrystalline nanostructure in the studied rod-shaped part along a diameter of the irradiated cross-section of the rod.

2 Experimental

Highly oriented polyethylene (PE) rods of 6 mm diameter are prepared by high-pressure injection moulding (HPIM) [2,27] from commercial material. Anticipating a demonstration study of X-ray micro-CT, one of the rods is warm-drawn in order to both reduce its diameter and to hopefully introduce some complex shell structure. A cross-section from the neck region is studied by micro-CT at the materials science beamline BW4 of HASYLAB, Hamburg. In order to obtain a modest spatial resolution, the primary beam has been focused on the sample by means of a stack of Beryllium lenses [6–8]. During the tomographic scan 7000 SAXS patterns are recorded on a two-dimensional (2D) detector. From this set of projections the SAXS images related to the irradiation of individual volume elements (voxels) in the studied cross-section are computed by tomographic back-projection [21]. A sequence of SAXS images from a diameter of the studied fibre cross-section is finally subjected to a quantitative analysis of the nanostructure.

Commercial high-density, low-branched Ziegler-Natta type polyethylene (PE) is used for our experiments (Lupolen 6021 D, BASF, M_W=182000 g/mol, M_n=25000 g/mol, density 0.962 g/cm^3, melt flow index 0.2).

Rods (6 mm diameter, 10 cm length) are prepared using the HPIM [2, 27] process in order to obtain a material with high preferential orientation. An equilibrated, low-temperature melt (150°C) is injected under high pressure into a cold mold. Maximum mold pressure is 400 MPa and final mold pressure 350 MPa after 180 s. In the differential scanning calorimetry (DSC) the material exhibits bimodal melting with peak maxima at 131°C and 141°C.

Warm-drawing of the PE rod is performed at approx. 80°C in an extensometer (Zwicki Z1.0/TH1S, Zwick Ltd, Ulm, Germany) at a speed of 1 mm/min. Necking with only little narrowing from 6 mm to 5 mm diameter is observed.

Micro-CT SAXS measurements are carried out at beamline BW4. The incident primary beam is focused by means of a stack of Be-lenses yielding a beam cross-section at the sample of 57 μm integral width and 39 μm height. The distance sample-detector is 1871 mm. The resolution of the optical setup is equivalent to a Bragg-spacing of 150 nm. Scattering patterns are exposed for 20 s using a 2D marccd 165 detector (mar research, Norderstedt, Germany).

Detailed information on the tomographic setup and the conversion of the recorded projection data to SAXS slice data has already been published [21]. It appears worth to be noted that the absorption factor is constant over the studied cross-section of the material. Thus the presence of macroscopic voids can be excluded, and the density variation inside the material is low.

3 Data Evaluation

The nanostructure analysis of the reconstructed SAXS patterns has been carried out by means of computer programs written in *pv-wave* [28]. The sources are available for download on the web [29].

Technical Data of the Reconstructed SAXS Patterns. Reconstructed patterns are obtained in 128 × 128 pixel, 16-bit TIFF-format. With respect to reciprocal space each pattern maps a volume equivalent to $-0.16\,\mathrm{nm}^{-1} < s_{12}, s_3 < 0.16\,\mathrm{nm}^{-1}$ with $\mathbf{s} = (s_{12}, s_3)$ in cylindrical coordinates and the norm $s = \sqrt{s_{12}^2 + s_3^2} = (2/\lambda)\sin\theta$. 2θ is the scattering angle. s_3 is in the direction of the fibre axis (meridian). The linear sequence of patterns describes the SAXS emanating from 70 consecutive voxels (index: 00 to 69) on a diameter of the irradiated fibre cross section. The

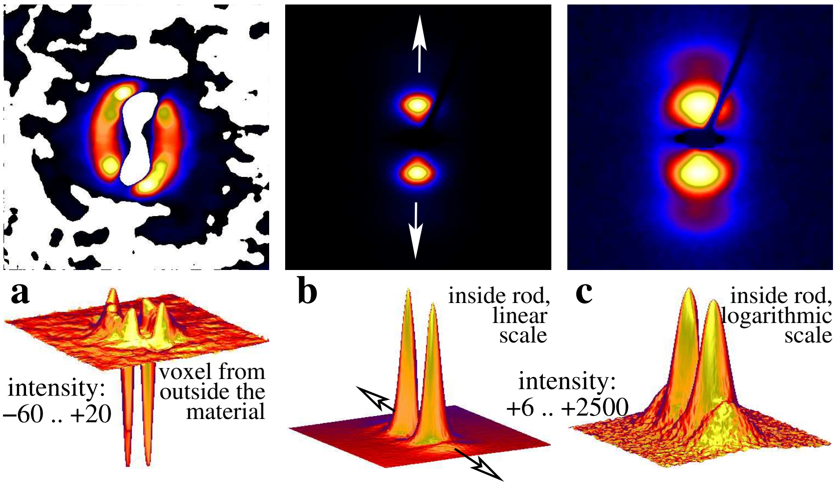

Figure 1: Original SAXS patterns (pseudo-colour and 3D plot) from different voxels obtained by micro-CT reconstruction from measured SAXS projection patterns of a PE rod. Each image shows a region -0.15 nm^{-1} $\leq s_{12}, s_3 \leq$ 0.15 nm^{-1}. Arrows indicate the fibre axis s_3

voxel size is 80 μm. It is defined by the step size of sample translation during the experiment.

Figure 1 shows two typical reconstructed SAXS patterns. In Figure 1a reconstructed “SAXS data” from an invalid voxel outside the fibre (voxel 00) is presented to demonstrate the typical amount of artifacts. Reconstructed SAXS from a valid voxel (06) is displayed in Figure 1b, c. Figure 1b shows the pattern on a linear scale, Figure 1c represents the same data set on a logarithmic intensity scale. The beam stop and its holder are clearly visible and the corresponding areas can be marked as invalid. Most of the reconstructed SAXS patterns show a similar quality concerning the signal-to-noise ratio.

Preparation of the SAXS Data. The broad SAXS reflections of the polymer are sufficiently resolved even on the coarse grid that was chosen to save reconstruction time. For the purpose of nanostructure analysis by means of the CDF method [26] the images are blown up to 512 × 512 pixels by 2D interpolation using biquadratic polynomials. Blind areas from the primary beam stop are masked. Misalignment of the raw images is corrected.

From SAXS Patterns to CDF. The next steps of data evaluation are illustrated in Figure 2. Figure 2a demonstrates the result of pattern harmonisation. Blind areas have been filled from symmetry considerations and the data in each quadrant have been averaged.

Figure 2b shows the scattering intensity $I(s_{12}, s_3)$ after filling the remnant central hole by 2D extrapolation utilising radial basis functions [30]. This pattern is the fundament of a model-free nanostructure visualisation and analysis in real space.

For nanostructure analysis we anticipate the study of a real-space function that is a slice but not a projection and bear in mind that in reciprocal space the fibre-symmetrical function $I(s_{12}, s_3)$ may be considered as a slice, e.g. $I(s_1, s_3)$. Utilising the Fourier-slice theorem we thus prepare to study a real-space slice by projecting in reciprocal space

$$\{I(s_{12}, s_3)\}(s_1, s_3) = \int I(s_{12}, s_3)\, ds_2.$$

The result is shown in Figure 2c. A 2D Fourier transform of this projected function would be proportional to a 2D slice of the multidimensional correlation function, $\gamma(r_{12}, r_3)$ [31].

Because the features of the nanostructure are difficult to distinguish in a correlation function, we carry out edge-enhancement of the nanometre size domains by application of the real-space Laplacian. In reciprocal space this is equivalent to a multiplication by $-4\pi^2 s^2$ [26]. Following a traditional convention on the definition of interference functions, [32] we here cancel the negative sign. The interference function requires background subtraction according to Porod's law. In the multidimensional case the background is suitably defined by low-pass spatial-frequency filtering of the pattern obtained sofar [26]. The determined background is subtracted. In principle this process of filtering and subtraction may be iterated until the integral of the determined interference function is vanishing. Such recursion should be avoided if possible, because it eliminates the effects of domain surface roughness and erases the scattering effect of small domains from the CDF [26]. Nevertheless, the first application of the filter rarely returns a proper function that is vanishing for large $\mathbf{s}$. Thus, in general, we apply the low-pass filter twice, and the interference function $G(s_{12}, s_3)$ is obtained. Figure 2d shows $|G(s_{12}, s_3)|$ in a pseudo-colour representation on a logarithmic scale. Extinguished in $G(s_{12}, s_3)$ are tomographic reconstruction errors of the SAXS intensity that result in slowly varying backgrounds. Finally the multidimensional

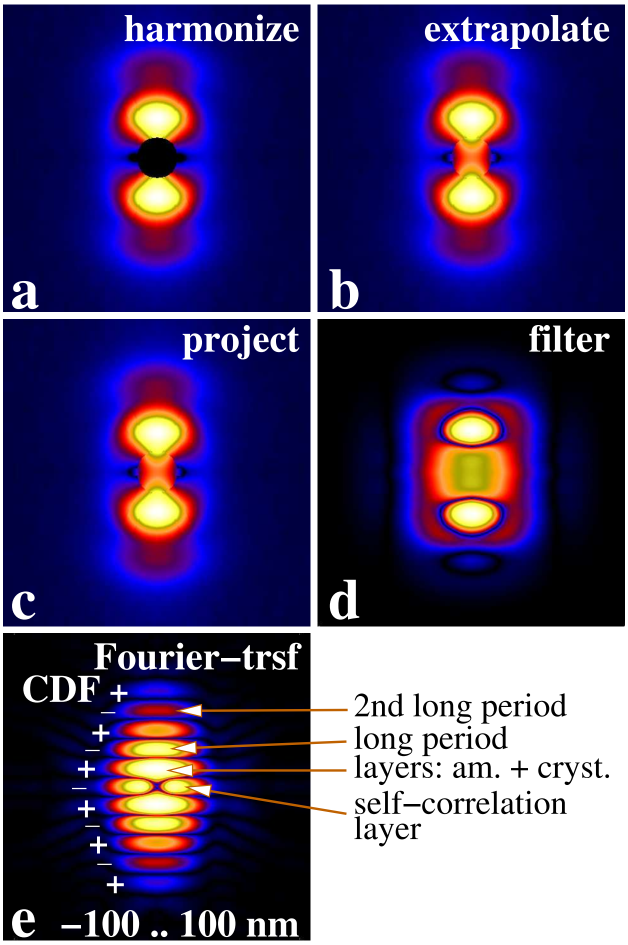

Figure 2: Conversion of SAXS to CDF. All pseudo-colour data on logarithmic intensity scale. (a)-(d) show a region -0.15 nm^{-1} $\leq s_{12}, s_3 \leq$ 0.15 nm^{-1}. Fibre axis (s_3) is vertical. (a) SAXS after filling blind areas in Figure 1c from harmony considerations. (b) After filling the centre by 2D extrapolation. (c) Projection on the representative fibre plane (d) Interference function (absolute values shown) by spatial frequency filtering. (e) CDF (absolute values; original sign of peaks labelled) by 2D Fourier transform. Some characteristics of the nanometre size layer system are indicated. The horizontal extension of the self-correlation layer is a measure of the extension of the lamellae from inside the voxel

CDF

$$z(r_{12}, r_3) = \mathcal{F}^2(-G(s_{12}, s_3))$$

is received by 2D Fourier transformation. Figure 2e shows $|z(r_{12}, r_3)|$ in a pseudo-colour representation on a logarithmic scale. The map fills a volume of reciprocal space equivalent to $-100\,\mathrm{nm} < r_{12}, r_3 < 100\,\mathrm{nm}$.

Discussion of a CDF. The fundamental ideas of an interpretation of the CDF are discussed in the following paragraph. Here we will shortly introduce the main features of a practical CDF describing a semicrystalline nanostructure with fibre symmetry (Figure 2e). The pattern is always symmetric about the equator. It describes a nanostructure made from crystalline and amorphous domains. The height of the CDF signal is proportional to the area of *surface* contact between the domains of the nanostructure and those of its imagined displaced ghost as a function of the displacement, $\mathbf{r}$. On the equator of the CDF we observe the self-correlation triangle, if a layer system is present. Its centre is always depressed from the mathematics of background subtraction ($z(0) \approx 0$). The next "layer line" shows up with positive sign. It is related to the correlation of the "upper" surface of a lamella with its "lower" surface. In the data of the present study the layer thickness distributions are always strongly overlapping. Therefore the crystalline layer thicknesses cannot be visually discriminated from the layer thickness distributions of the amorphous layers. Thus the second off-equator layer line is related to the long period. It shows up with negative sign. Even the 2nd-order long-period can be distinguished in the pattern. This feature demonstrates that the longitudinal correlation among the crystalline lamellae from a stack is not too bad: 3 crystalline lamellae are correlated and form a stack.

The discussion of the CDF in terms of the nanodomain topology [2, 26, 33, 34] within the sample is straightforward, since the CDF is defined [26] by the Laplacian of Vonk's multidimensional correlation function [31]. As such it presents the autocorrelation of the surfaces from the (nanometre size) domains in space in a similar manner as Ruland's interface distribution function does [35–37] for one–dimensional structures as a function of distance. For samples with fibre symmetry, the CDF $z(r_{12}, r_3)$ is a function of two coordinates only (lateral direction r_{12}, and fibre direction r_3). Therefore it can be displayed in a plane. Positive peaks found in the vicinity of the origin are size distributions of the primary domains. Thus their size, shape and orientation in space are depicted. Negative peaks following farther out exhibit "long periods", i.e. the distance of two adjacent domains from

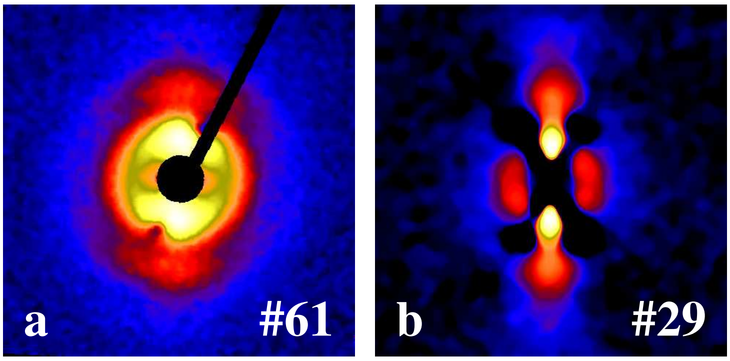

Figure 3: The two types of unusual SAXS patterns observed in some voxels (voxel number indicated). Each raw SAXS pattern describes a volume in reciprocal space -0.15 $\mathrm{nm}^{-1} \leq s_{12}, s_3 \leq 0.15\ \mathrm{nm}^{-1}$. Fibre axis ($s_3$) is vertical. (a) shows the SAXS of a voxel containing the superposition of two patterns with different orientation. The strong pattern is coincident with the macroscopic fibre axis. (b) shows a pattern which can be explained by a superposition of extended chain crystals and lamellae stacks

each other. Subsequent positive peaks describe the size and orientation of superdomains (i.e. assemblies made from two primitive domains separated by a rather probable distance), and correlations among domains more distant are manifested in consecutive peaks at longer distance.

4 Results and Discussion

4.1 Peculiar Scattering Patterns and Imaging Errors

Scattering patterns from a few voxels are peculiar, and the two kinds of observed peculiarities are illustrated in Figure 3. Figure 3a looks like a superposition of two fibre patterns with different orientation. We are irritated by the fact that the respective patterns (voxels 8, 9, 60, 61, 62) exhibit a small but clear deviation from fibre symmetry. We have expected that fibre symmetry should have been imprinted on the contents of every voxel by averaging, because during scanning the sample is rotated about an axis – in analogy to the classical rotation-crystal method. In other words, each physical voxel is irradiated from all directions in the studied cross-section plane of the sample. We speculate that the adjusted mismatch between a smaller physical voxel size and a bigger translational step-size makes the reconstructed SAXS pattern sensitive to structure gradients within the computational voxel defined by the step size. In this case the observation could be indicative for a shear-zone, in particular because the effect is observed in two clusters of voxels situated at the same distance (2.1 mm) from the central core of the studied rod. Physically a corresponding shear-zone may have been the result of the sample preparation by warm-drawing. Indication for this interpretation is founded on visual inspection of the failure zone in the neck of the rod that showed pull-out of a central core of approx. 4 mm diameter.

Figure 3b exhibits the other unusual type of scattering pattern. Discrete equatorial scattering (peaks on the equator or indented pairs of peaks) is observed in SAXS patterns from the central zone of the rod. In contrast to the artifact patterns from outside the sample (cf. Figure 1a) the intensity is high enough to be significant. As the voxel position is further approaching the core of the fibre, first the meridional reflections and later the equatorial ones are vanishing. An analysis of the structure by means of the CDF is impossible. Such scattering patterns can be interpreted by a structural model in which the meridional reflections are caused from lamellae stacks, whereas the equatorial features are caused from elongated domains (extended-chain crystals, “shish”) with a preferential distance between them. In this case tilted equatorial reflections as in Figure 3b indicate that not all of the principal axes of the extended-chain crystals are parallel to the macroscopic fibre axis of the studied material. In Figure 3b we also observe a serious anomaly: a large X-shaped region (colour: black) in which the reconstructed intensity drops to negative values. This imaging error is, in fact, a shortcoming of the reconstruction algorithm at this early stage of development that must be improved in the future.

In Figure 4 the reconstructed scattering patterns are documented on the same logarithmic intensity scale. The chosen representation makes data from voxels 5 and 6 appear overexposed for the sake of a clear documentation of imaging errors. Scattering patterns marked by an arrow are subjected to a considerable amount of reconstruction error with the arrow pointing to the region exhibiting negative reconstructed SAXS intensity. The scattering patterns from the second half of the reconstructed cross-section look very similar with different amounts of reconstruction flaws. Visual inspection yields that the patterns from voxels 4–13 can be accepted as common SAXS patterns. The patterns from voxels 14–31, on the other hand, show at least tiny spots of an anomalous 4-point intensity depression

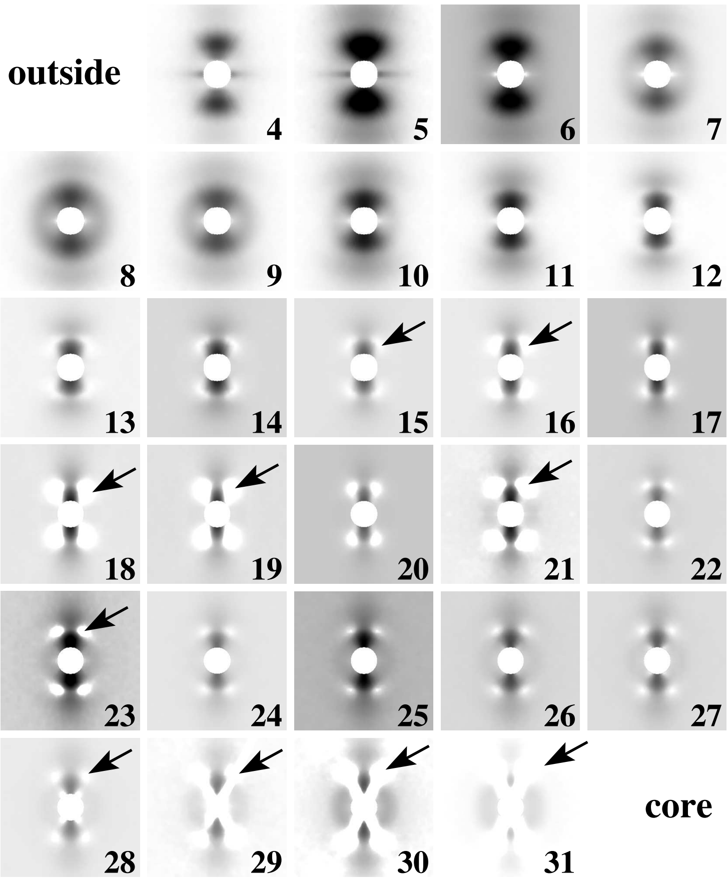

Figure 4: Radial variation of SAXS in a cross-section of an injection molded PE rod. Central part of the reconstructed intensity $\log(I(\mathbf{s}))$ (-0.1 $\mathrm{nm}^{-1} \leq s_{12}, s_3 \leq$ 0.1 nm^{-1}. Fibre axis (s_3) is vertical). Voxel index 4: rod surface, $i_v = 34.5$: centre of the rod. Arrows indicate regions in some patterns in which an anomalous intensity decrease is observed

which becomes a large x-shaped depression zone for voxels 29–31. As observed, the most severe effect of the reconstruction error is a background: If a very broad Gaussian would be added to the reconstructed intensity, it would appear like a usual SAXS pattern.

4.2 A Pathway for the Elimination of Imaging Errors

In tomography, in general, imaging errors are expected at the beginning of the method development. The history of tomography for other applications has shown that such artifacts can be minimised in an iterative process, until faithful images are obtained by filtered backprojection [18]. Repeating the historical proceeding, the reconstruction of known virtual structures ("phantoms") can be compared to the phantom itself. Finally it should be possible to adjust the reconstruction algorithm iteratively. In this respect it appears most promising to focus on two program modules. The first is the filter module of the reconstruction algorithm. The second module is the tomographic model of the sample that is presently used. It presently assumes perfect fibre symmetry and one could try to extend it.

What can we do at this early stage of development? Ultimately we are not interested in a faithful reconstruction of SAXS intensity. Instead, we intend to gather information on the nanostructure of the material. Thus here we try first to circumvent the task to heal the obvious artifacts in some of the SAXS patterns by switching to a different representation on nanostructure.

Such a representation is the multidimensional chord distribution function (CDF) [26, 38]. It is not sensitive to a wrong, slowly varying background in the SAXS pattern because the SAXS background is removed anyway as the interference function is computed.

If then we obtain a consistent view on nanostructure as a function of position in our material, the returned result of yet unknown significance is at least a reasonable virtual volume-resolved phantom structure. With some programming effort this structure may later be converted into an analytical mathematical description. Then the tomographic scan can be simulated by integration. The result is a virtual set of SAXS patterns that can be looped back into the reconstruction algorithm. Finally, the tomographic model and the filters of the reconstruction algorithm are adjusted until the reconstruction result is best-matching the phantom structure. At this anticipated stage even the SAXS intensity of the phantom structure should be reproduced faithfully, and the fidelity of the method were finally established.

4.3 CDFs – from Surface to Core

As we now compute the CDFs from the reconstructed SAXS patterns we assume that the *only* relevant effect of the imaging error on the reconstructed SAXS intensity is a slowly varying background. This assumption is a first approximation. Nevertheless there may be higher-order effects introducing artifacts into the CDF. Figure 5 documents the apparent nanostructure variation from the surface to the centre of the studied rod in the CDFs. Not shown is the other half of the evaluated CDF data, because it essentially constitutes a mirrored copy of the shown patterns. From the voxel index i_v and the lateral size of each voxel the position $x_{12} = |i_v - 34.5| \times 0.08\,\mathrm{mm}$ of each voxel on the rod diameter is readily assessed.

The first voxel below the rod surface (Figure 5, $i_v = 4$) exhibits a nanostructure with a good longitudinal correlation (7 lines are crossing the meridian, i.e. the stack of crystalline lamellae is comprising 4 correlated lamellae). Moreover, the lines are rather long in equatorial direction. This shows that the lateral extension of the lamellae is big.

In the following two voxels both the lateral extension of the lamellae and the longitudinal correlation among them are decreasing. This may be addressed as a gradual change from a layer stack towards a microfibrillar system. Beginning from voxel 8 an increase of lateral correlation with neighbouring domains is detected. Thus the shift from a lamellar towards a microfibrillar system does not end in random placement of microfibrils. Instead, a preferential distance among them is established in lateral direction as well ("macrolattice" of Wilke and Fronk [39,40]). Up to this point in the abovementioned "shear-zone", the nanostructure is a unimodal system. Beyond this zone the CDF exhibits two nanostructural components. We observe a layer system with layers of, again, increasing lateral extension accompanied by a distinct microfibrillar component with its typical narrow peaks at the meridian and a long period that is only half of the long period of the lamellar component. By visual inspection of the intensity $I(\mathbf{s})$ no artifacts are detected up to voxel 13. In the CDF representation a continuous variation of structure is observed across this border at which artifacts become visible in $I(\mathbf{s})$. This observation indicates that the second-order effects of imaging errors on $I(\mathbf{s})$ may be small and negligible in the CDF.

A second break-down of lateral layer size is clearly observed at voxels 19 and 20. In this two CDFs even the layer peaks appear to be modulated – a block-structure according to the notion put forward by Strobl [41] is encountered. It appears worth to be noted that the imaging error is considerable for voxel 19 but small for voxel

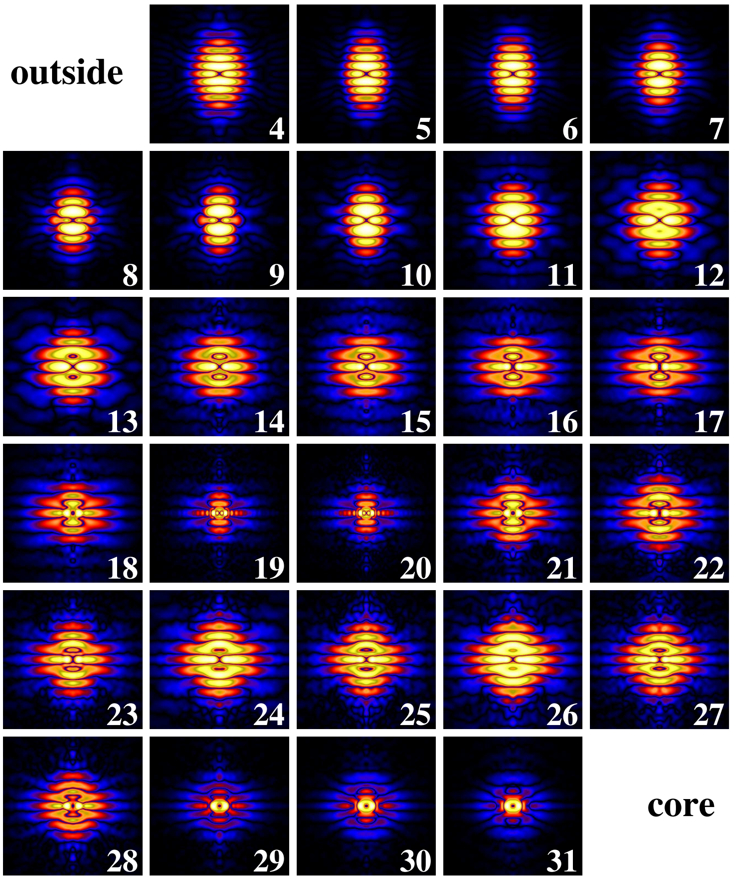

Figure 5: Radial variation of nanostructure in a cross-section of an injection molded PE rod as exhibited in the absolute CDF , $|z(\mathbf{r})|$ (-100 nm $\leq r_{12}, r_3 \leq$ 100 nm. Fibre axis (r_3) is vertical). CDFs computed from local SAXS patterns reconstructed by X-ray micro-CT. Voxel index 4: rod surface, $i_v = 34.5$: centre of the rod

20. Nevertheless the computed CDFs are very similar to each other but different from their neighbours. Unfortunately the feature corresponding to the CDF blocks in the SAXS data ("vertical walls of intensity" in the interference function) are at the edge of the detector window. Therefore the modulation effect of the blocks to the CDF is strongly dependent on the extrapolation chosen. Thus a discussion of block size, block distance and block arrangement is impossible. To overcome this problem the distance sample-detector should be elongated.

In the blocky zone the long period of the lamellae stacks takes its maximum in the material. Beginning from voxel 20 the long period starts to decrease, whereas the lateral extension of the layers is recovering, again. Finally the voxels 29 to 31 represent the region where lamellae and extended-chain crystals are co-existing. The strength of this feature is probably overemphasised by the severe X-shaped imaging error in $I(\mathbf{s})$. In the centre, beyond voxel 31, only weak equatorial scattering is observed and the CDFs cannot be analysed.

4.4 Results of Quantitative Analysis

Figure 6 displays nanostructure parameters as obtained by quantitative analysis of the peaks from the CDFs. Here the data for all voxels (00–69) of the analysed fibre diameter are presented in order to document symmetry and reproducibility. Data show that a lamellar-stack structure is present in a very broad zone of the fibre with the long period (filled triangles) showing a maximum of 38 nm at a distance of $|x_{12}| = 1.2$ mm from the core. Here and at $|x_{12}| = 2$ mm break-down zones of the lamellae extension (filled circles) are observed. Except for these breakdown-zones and the surface layer the lamellae extension is increasing towards the centre of the rod. In the range 0.5 mm $< |x_{12}| <$ 2 mm the nanostructure is bimodal with an additional microfibrillar component. The long period of the microfibrils (open triangles) is almost constant at 18 nm. The lateral extension of the domains that form the microfibrils (open circles) exhibits a maximum of 19 nm at $|x_{12}| = 1.2$ mm. The thinnest microfibrils are found at the borders of the interval-of-presence with diameters down to 6 nm.

In principle it is possible to determine more nanostructure parameters from the volume-resolved scattering data. The average thicknesses of layers and domains as well as the corresponding widths of layer and domain thickness distributions may be determined by model fitting to the CDF [27, 42, 43]. In this way an in-depth understanding of the nanostructure in a rod or a polymer fibre as a function

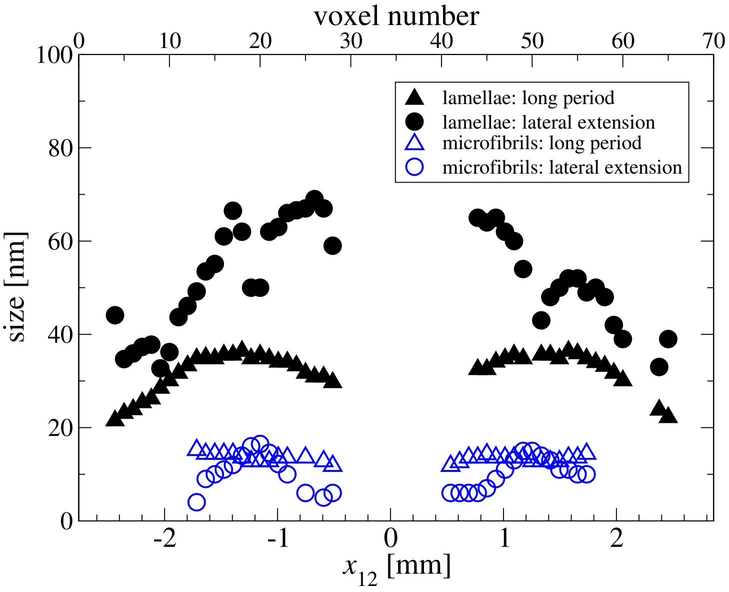

Figure 6: Radial variation of nanostructure parameters in the studied cross-section of the PE rod material. Values are determined from positions and extensions of the peaks in the multidimensional CDF $z(r_{12}, r_3)$ as presented in Figure 5

of volume may be obtained by the applied non-destructive method as soon as the tomographic reconstruction method has been fully validated.

For comparative routine studies of nanostructure variation in space even the analytical effort demonstrated here might not be necessary. A more effective pathway would restrict an in-depth analytical study to a reference material in order to identify respective zones in an imaging tomogram. Comparison of imaging tomograms of similar materials would then probably be sufficient to establish basic relations between materials processing parameters and the volume distribution of nanostructure. In the following section such a relation between the analysed structure and an imaging tomogram of our sample shall be established, but before that an example of a relation between structure and processing shall be given.

If spun fibres were studied by micro-CT SAXS, one could correlate, e.g., the observed width of the extended-chain-core to parameters like die geometry, melt temperature, molecular weight, draft and take-up speed. Similar could be done with the unimodal lamellar morphology which in our material is restricted to a peripheral zone. If, in an ultimate case, the whole fibre were filled by a unimodal lamellar zone the material would probably share the mechanical properties of a hard-elastic [44–48] material.

4.5 Nanostructure and the Zones of an Imaging Tomogram

In a previous paper [21] we have already published an imaging tomogram of the studied material. It was obtained by assigning to each voxel a grayscale value

$$c(x_1,x_2) = \int I(s_{12}=0,s_3,x_1,x_2)\,ds_3$$

that is proportional to the integral of the scattering intensity on the meridian. Thus the one-dimensional intensity slice $\lceil I(\mathbf{s}) \rceil_1 (s_3) = I(s_{12}=0,s_3)$ has been projected to a zero-dimensional number $\{\lceil I(\mathbf{s}) \rceil_1 (s_3)\}_0$ that is chosen to represent the brightness of each voxel (x_1,x_2).

The zones identified in the present nanostructure analysis are readily related to the features of the imaging tomogram (Figure 7). Without any information on nanostructure in the sample, the imaging SAXS micro-CT visualises a sequence of distinct circular zones in the material. In Figure 7 they are indicated by a sequence of dots labelled by the voxel numbers. Because widths and positions of these zones are identical to the characteristic zones of the present CDF analysis, an assignment is straightforward.

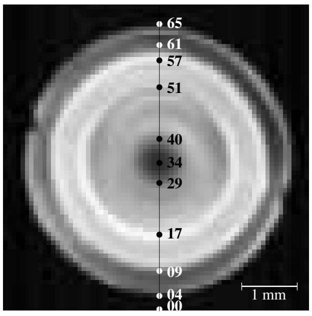

Figure 7: Imaging tomogram prepared from the SAXS data of the studied PE rod. The evaluated vertical section is indicated. Voxel numbers of characteristic voxels are indicated

5 Conclusion

As has been demonstrated in this study, the reconstructed SAXS patterns from a micro-CT experiment contain much more information than a grayscale value that can be computed to identify different zones in a polymer part with a nanostructure gradient. Nevertheless, the zones of the imaging tomogram are faithfully indicating the zones of different nanostructure in the “fibre” that are found by the more involved CDF analysis presented here. Thus for the purpose of scanning different but similar materials the micro-CT SAXS image will often be sufficient. This should in particular become true, if the explanatory power of the imaging tomogram is increased by retrieving three significant numbers from the SAXS pattern and combining them into a pseudo-*colour* tomogram.

On the other hand, for more in-depth studies of nanostructure variation in volume the combination of SAXS micro-CT and a quantitative nanostructure analysis of the reconstructed SAXS patterns promise to become a powerful tool. As soon as the imaging errors are extinguished, it will be possible to study nanostructure variation in materials with a spatial resolution that is inaccessible to a conventional slicing-and-irradiation procedure. It can be expected that the technical progress of synchrotron beamlines will soon result in the general availability of scanning setups with a spatial resolution [3, 49] of 2 μm and less which permit to study the spatial nanostructure variation inside single polymer filaments as a function of processing parameters.

With respect to tomographic reconstruction of SAXS the presented work is only a first step. Much more effort has to be spent in order to make SAXS tomography a reliable and tool. For this purpose a long-term cooperation of software engineers and scientists in a development group should be installed at some synchrotron radiation facility. In the long run even other methods (like the CDF method) could profit from the work of such a group that were aiming at optimisation and standardisation of visualisation software based on Fourier transformation techniques. With respect to user service such a group could set up a tomographic reconstruction facility. In this case the user could be served with volume-resolved SAXS patterns or CDFs at the radiation facility. Besides the direct profit for materials science, the work of such a group would generally increase the acceptance of Fourier transformation methods in the scientific community.

Acknowledgement. We acknowledge HASYLAB, Hamburg, for provision of the synchrotron radiation facilities at beamline BW4. Financial support by the Deutsche Forschungsgemeinschaft (DFG STR501/4-1) is gratefully acknowledged. The development of refractive X-ray lenses is supported by the German Ministry of Education and Research (BMBF grant 05KS4PA1/9). In particular we acknowledge the support of Dipl. Ing. F. Tschöpe concerning the high-pressure injection-moulding and the support of the HASYLAB engineers R. Döhrmann and M. Dommach before and during the beamtime.

References

[1] N. Stribeck, S. Buchner, *J. Appl. Cryst.* **1997**, *30*, 722.

[2] N. Stribeck, R. Bayer, G. von Krosigk, R. Gehrke, *Polymer* **2002**, *43*, 3779.

[3] C. Riekel, P. Engström, *Nuclear Instr. Meth. Phys. Res.* **1995**, *B97*, 224.

[4] T. A. Waigh, A. M. Donald, F. Heidelbach, C. Riekel, M. J. Gidley, *Biopolymers* **1999**, *49*, 91.

[5] R. Kolb, C. Wutz, N. Stribeck, G. v. Krosigk, C. Riekel, *Polymer* **2001**, *42*, 5257.

[6] B. Lengeler, J. Tümmler, A. Snigirev, I. Snigireva, C. Raven, *J. Appl. Phys.* **1998**, *84*, 5855.

[7] B. Lengeler, C. G. Schroer, B. Brenner, T. F. Günzler, M. Kuhlmann, J. Tümmler, A. S. Simionovici, M. Drakopoulos, A. Snigirev, I. Snigireva, *Nucl. Instrum. Methods Phys. Res. A* **2001**, *467-468*, 944.

[8] C. G. Schroer, M. Kuhlmann, B. Lengeler, T. F. Günzler, O. Kurapova, B. Benner, C. Rau, A. S. Simionovici, A. A. Snigirev, I. Snigireva, *Proc. SPIE* **2002**, *4783*, 10.

[9] B. Lengeler, C. G. Schroer, M. Kuhlmann, B. Benner, T. F. Günzler, O. Kurapova, F. Zontone, A. Snigirev, I. Snigireva, *J. Phys. D: Appl. Phys.* **2005**, *38*, A218.

[10] B. Lengeler, C. Schroer, J. Tümmler, B. Benner, M. Richwin, A. Snigirev, I. Snigireva, M. Drakopoulos, *J. Synchrotron Rad.* **1999**, *6*, 1153.

[11] P. Cloetens, W. Ludwig, J. Baruchel, D. v. L. van Dyck, J., J. P. Guigay, M. Schlenker, *Appl. Phys. Lett.* **1999**, *75*, 2912.

[12] A. S. Simionovici, M. Chukalina, C. Schroer, M. Drakopoulos, A. Snigirev, I. Snigireva, B. Lengeler, K. Janssens, F. Adams, *IEEE Trans. Nucl. Sci.* **2000**, *47*, 2736.

[13] C. G. Schroer, *Appl. Phys. Lett.* **2001**, *79*, 1912.

[14] B. Golosio, A. Somogyi, A. Simionovici, P. Bleuet, J. Susini, L. Lamelle, *Appl. Phys. Lett.* **2004**, *84*, 2199.

[15] C. Rau, A. Somogyi, A. Bytchkov, A. Simionovici, in: U. Bonse, Ed. “Developments in X-Ray Tomography III”, vol. 4503 of *Proceedings of the SPIE*, pp. 249–255, **2002** pp. 249–255.

[16] C. G. Schroer, M. Kuhlmann, T. F. Günzler, B. Lengeler, M. Richwin, B. Griesebock, D. Lützenkirchen-Hecht, R. Frahm, E. Ziegler, A. Mashayekhi, D. Haeffner, J.-D. Grunwaldt, A. Baiker, *Appl. Phys. Lett.* **2003**, *82*, 3360.

[17] C. G. Schroer, P. Cloetens, M. Rivers, A. Snigirev, A. Takeuchi, W. Yun, *MRS Bulletin* **2004**, *29*, 157.

[18] U. Bonse, F. Busch, *Prog. Biophys. Molec. Biol.* **1996**, *65*, 133.

[19] W. Treimer, A. Hilger, N. Kardjilov, M. Strobl, *Nucl. Instrum. Methods Phys. Res. A* **2005**, *542*, 367.

[20] S. J. Wilkinson, K. D. Rogers, C. J. Hall, R. A. Lewis, A. Round, S. E. Pinder, C. Boggis, A. Hufton, *Nucl. Instrum. Methods Phys. Res. A* **2005**, *548*, 135.

[21] C. G. Schroer, M. Kuhlmann, S. V. Roth, R. Gehrke, N. Stribeck, A. Almendarez Camarillo, B. Lengeler, *Appl. Phys. Lett.* **2006**, , in print.

[22] P. J. Schilling, B. R. Karedla, A. K. Tatiparthi, M. A. Verges, P. D. Herrington, *Compos. Sci. Technol.* **2005**, *65*, 2071.

[23] R. J. Spontak, M. C. Williams, D. A. Agard, *Polymer* **1988**, *29*, 387.

[24] Y. Ikeda, A. Katoh, J. Shimanuki, S. Kohjiya, *Macromol. Rapid Commun.* **2004**, *25*, 1186.

[25] H. Sugimori, T. Nishi, H. Jinnai, *Macromolecules* **2005**, *38*, 10226.

[26] N. Stribeck, *J. Appl. Cryst.* **2001**, *34*, 496.

[27] N. Stribeck, A. Almendarez Camarillo, S. Cunis, R. K. Bayer, R. Gehrke, *Macromol. Chem. Phys.* **2004**, *205*, 1445.

[28] VNI, “pv-wave manuals”, V 7.5 (2001), Boulder, Colorado.

[29] N. Stribeck, “Web Page”, http://www.chemie.uni-hamburg.de/tmc/stribeck/.

[30] M. D. Buhmann, *Acta Numerica* **2000**, *9*, 1.

[31] C. G. Vonk, *Colloid Polym. Sci.* **1979**, *257*, 1021.

[32] F. Zernike, J. A. Prins, *Z. Phys.* **1927**, *41*, 184.

[33] N. Stribeck, S. Fakirov, *Macromolecules* **2001**, *34*, 7758.

[34] N. Stribeck, E. Buzdugan, P. Ghioca, S. Serban, R. Gehrke, *Macromol. Chem. Phys.* **2002**, *203*, 636.

[35] W. Ruland, *Colloid Polym. Sci.* **1977**, *255*, 417.

[36] W. Ruland, *Colloid Polym. Sci.* **1978**, *256*, 932.

[37] N. Stribeck, W. Ruland, *J. Appl. Cryst.* **1978**, *11*, 535.

[38] N. Stribeck, *Anal. Bioanal. Chem.* **2003**, *376*, 608.

[39] W. Fronk, W. Wilke, *Colloid Polym. Sci.* **1983**, *261*, 1010.

[40] W. Fronk, W. Wilke, *Colloid Polym. Sci.* **1985**, *263*, 97.

[41] T. Hugel, G. Strobl, R. Thomann, *Acta Polym.* **1999**, *50*, 214.

[42] N. Stribeck, *Macromol. Chem. Phys.* **2004**, *205*, 1455.

[43] N. Stribeck, A. Almendarez Camarillo, R. Bayer, *Macromol. Chem. Phys.* **2004**, *205*, 1463.

[44] H. D. Noether, *Intern. J. Polymeric Mater.* **1979**, *7*, 57.

[45] H. D. Noether, W. Whitney, *Kolloid-Z. u. Z. Polymere* **1973**, *251*, 991.

[46] I. K. Park, H. D. Noether, *Colloid Polym. Sci.* **1975**, *253*, 824.

[47] T. Hashimoto, K. Nagatoshi, A. Todo, H. Kawai, *Polymer* **1976**, *17*, 1063.

[48] H. Zhou, G. L. Wilkes, *Polymer* **1997**, *38*, 5735.

[49] M. Müller, C. Czihak, G. Vogl, P. Fratzl, H. Schober, C. Riekel, *Macromolecules* **1998**, *31*, 3953.

Synopsis. We propose to study nanostructure gradients in advanced polymer materials in non-destructive experiments with high spatial resolution utilizing a combination of microtomography and small-angle X-ray scattering. Applied to an injection molded rod and analyzed by the chord distribution function method data reveal a central zone of extended chains surrounded by varying microfibrillar and lamellar nanostructure.